Device

Article

Full 2π phase modulation using exciton-polaritons in a two-dimensional superlattice

Graphical abstract

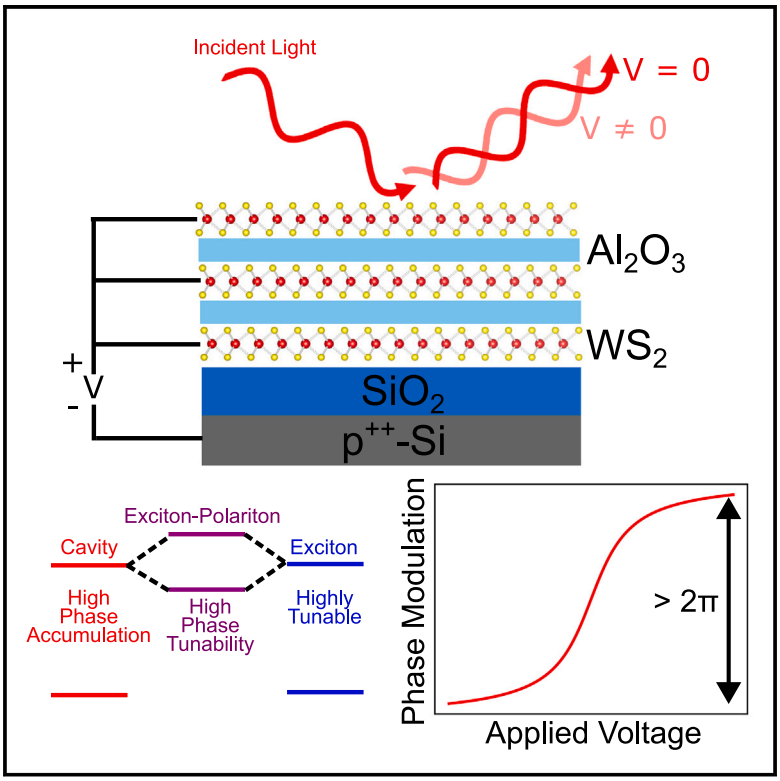

Highlights

- Electrostatic doping modulates the light-matter interactions of exciton-polaritons
- Full 2π phase modulation is achieved in an unpatterned superlattice
- Performance of 1D grating phase modulator is simulated

Authors

Jason Lynch, Pawan Kumar, Chen Chen, ..., Yu-Jung Lu, Joan Redwing, Deep Jariwala

Correspondence

dmj@seas.upenn.edu

In brief

Lynch et al. report a full 2π phase modulation of reflected light by electrostatically doping WS_2 monolayers within a superlattice. This was achieved by stacking monolayers of WS_2, which strengthened the light-matter interaction. These findings are vital for ultra-compact electro-optical systems such as phased arrays and visible light communication systems.

Lynch et al., 2025, Device *3*, 100639
January 17, 2025
Published by Elsevier Inc.
https://doi.org/10.1016/j.device.2024.100639

CellPress

Device

CellPress
OPEN ACCESS

Article

Full 2π phase modulation using exciton-polaritons in a two-dimensional superlattice

Jason Lynch,[1] Pawan Kumar,[1,2] Chen Chen,[3] Nicholas Trainor,[3,4] Shalina Kumari,[3,4] Tzu-Yu Peng,[5,6] Cindy Yueli Chen,[7] Yu-Jung Lu,[5,6] Joan Redwing,[3,4] and Deep Jariwala[1,8,*]

[1]Electrical and Systems Engineering, University of Pennsylvania, Philadelphia, PA 19104, USA
[2]Inter-University Microelectronics Center, Leuven 3001, Belgium
[3]2D Crystal Consortium Materials Innovation Platform, Materials Research Institute, Penn State University, University Park, PA, USA
[4]Materials Science and Engineering, Penn State University, University Park, PA, USA
[5]Research Center for Applied Sciences, Academia Sinica, Taipei 11529, Taiwan
[6]Graduate Institute of Applied Physics, National Taiwan University, Taipei 10617, Taiwan
[7]Department of Chemistry, University of Pennsylvania, Philadelphia, PA 19104, USA
[8]Lead contact
*Correspondence: dmj@seas.upenn.edu
https://doi.org/10.1016/j.device.2024.100639

THE BIGGER PICTURE Transition-metal-dichalcogenides (TMDCs) are used in photonics due to strong light-matter interactions and the ability to be thinned down to an atomic thickness. By stacking TMDCs with an insulator into a structure known as a superlattice, the TMDCs maintain their ideal electro-optical properties. These structures can be used as electro-optical modulators or phased arrays-type devices that change the phase and ultimately the direction of propagation of light upon the application of an electric field, important for sensing and telecommunication technologies. In this work, we enhanced the light-matter coupling strength and maintained the ideal monolayer properties by stacking TMDCs into a superlattice, enabling a higher degree of phase accumulation. The light-matter interaction was then modulated by electrostatic doping, and full 2π phase modulation of reflected light was observed. The full 2π modulation is vital for TMDCs unlocking ultra-compact, energy-efficient phased arrays and visible light communication systems.

SUMMARY

Active metamaterials promise to enable active control over the propagation of wavefronts of light for applications such as beam steering, optical communication modulators, and holograms. Current commercial devices use active layers that are several wavelengths thick to modulate the phase of light, which limits their compactness and energy efficiency. In atomically thin optics, the phase has been modulated using a resonant mode such as a plasmon or high-Q cavity mode that enable light to accumulate a large amount of phase over a short distance and coupling it to an active material. Here, we report that electrostatic doping can modulate the light-matter interaction strength of a two-dimensional WS2-based multi-quantum-well (MQW) structure going from strongly coupled, phase-accumulating exciton-polaritons to weakly coupled exciton-trion-polaritons. This transition leads to 2.02π radians of phase modulation being observed. This result demonstrates the potential of the MQW structure as a compact, lightweight electro-optical modulators for light detection and ranging (LiDAR) and optical communications in the visible range.

INTRODUCTION

As one of the quintessential classes of two-dimensional (2D) semiconductors, transition-metal-dichalcogenides (TMDCs) of Mo and W have shown potential to facilitate flat-optical systems[1,2] such as beam steering,[3] metalenses,[4] and electro-optical modulators.[5,6] Additionally, their large band gaps are ideal for visible light communications (VLCs)[7] and holography.[8] The direct band gap nature of TMDCs in the monolayer limit[9] and their large refractive index[10] are ideal for efficient, subwavelength photonics applications. Additionally, their strong excitons (i.e., coulomb-bound electron-hole pairs) in the visible and near infrared ranges[11] host strong light-matter interactions. The strength of these excitons depends heavily on the binding

energy of the constituent electron and hole pairs,[12] and, therefore, the light-matter interactions within TMDCs can be modulated by controlling the free-carrier concentration, which alters the binding energy.[13,14] Through the tuning of the exciton binding energy, multiple TMDCs have shown highly gate-tunable, complex refractive index ($\tilde{n} = n + ik$) values,[15–17] which is highly sought after in electro-optics.

Phase modulators such as those based on Si,[18] liquid crystals,[19] and III-V semiconductors,[20] rely on modulating their optical phase length to control the phase of light resulting in these modulators being bulky films. For instance, liquid crystals exhibit excellent performance as a phase modulator; however, their interaction length is several wavelengths long. Additionally, modulation of light requires the physical rotation of the liquid crystal molecules. This physical movement of the massive liquid crystals, instead of lightweight electrons and holes, increases the energy, slows the switching speed, and reduces the durability of the modulator. In contrast to bulky modulators, basic TMDC-based phase modulators rely on tuning bare excitons and trions in atomically thin layers to modulate the amplitude and phase of reflected light, and they use the injection of electrons or holes, which cut down on the switching energy and increase the switching speed. Recently, phase modulation of incident light up to $\pi/5$ radians has been demonstrated in monolayer TMDCs purely using the exciton resonance and the relatively slow ion gel gating method.[21] However, a single resonance cannot induce a phase shift greater than π. Instead, a second resonance is required for full 2π phase modulation of light, which is vital for applications such as phased arrays. It is common to do this by coupling excitons to a cavity mode to form part-matter, part-light quasiparticles called exciton-polaritons.[22,23] In this case, the cavity mode confines the light and causes it to accumulate a large degree of phase in a small volume while the exciton provides tunability.

Excitons have been coupled to waveguide modes in the past,[24,25] but previous phase modulators using TMDCs have focused on coupling to plasmon-polaritons.[6,26–28] However, the use of plasmonics increases the loss of the TMDC-plasmon-polariton system, and the exciton tunability should decrease along with its binding energy when it is placed in proximity with a metal.[29] In our previous work, we demonstrated a multi-quantum-well (MQW) or superlattice of WS_2 separated by insulators on top of a reflective substrate to form strongly coupled exciton-polaritons,[30] and other works have further confirmed the enhanced light-matter interactions in TMDC/insulator superlattices.[31–33] The 3-nm thickness of the insulating layers is enough to electronically isolate the WS_2 monolayers,[34] allowing them to keep the direct band gap characteristics including the large exciton binding energy[35,36] while increasing the light-matter interactions. Since the TMDCs maintain their large binding energy, they also maintain their high tunability, which can be leveraged to produce highly efficient, compact phase modulators using exciton-polaritons.

In this work, we demonstrate that exciton-polaritons enable full 2π phase modulation in a superlattice of WS_2 and Al_2O_3 on a SiO_2/Si substrate. Instead of forming an external cavity using top and bottom reflectors or nanopatterning, self-hybridized, strongly coupled exciton-polaritons form under transverse electric (TE) polarized light at an angle of incidence (AOI) of 55°. The light-matter interaction strength is tuned using electrostatic doping, and the exciton and trion coupling parameters are modulated by −23% and +129%, respectively. Leveraging the fact that the phase of transverse magnetic (TM) polarized light is unaffected by electrostatic doping, spectroscopic ellipsometry is used to experimentally verify that 2.02π phase modulation is occurring. Although the loss of the phase modulator remains large, it achieves full control of the phase of light, which is vital for light detection and ranging (LiDAR) and free-space optical communications.

RESULTS

Fabrication of superlattice

Large-area monolayers of WS_2 are grown using a metal-organic chemical vapor deposition (MOCVD) technique, which has been shown to produce films with excellent electrical properties.[37,38] A wet-transfer technique is used to transfer centimeter-sized monolayers on to the SiO_2/Si, and atomic-layer deposition (ALD) is used to deposit the Al_2O_3 insulating layers to fabricate the superlattice (details regarding the experimental procedures can be found in Figure S1). Al_2O_3 is chosen as the insulator instead of other dielectrics such as hBN because the ALD process produces no contaminants during the fabrication process without affecting the light-matter coupling strength and because we did not observe exciton linewidth narrowing in previous large-area WS_2/hBN superlattices[30] (see Figure S2).

In addition, ALD is a widely adopted thin-film process in microfabrication across all semiconductor foundries. The wet transfer technique has been shown to maintain the high electrical quality of the monolayers.[37,39] The electrical contact (10 nm of Ti and 40 nm of Au) is deposited to make electrical contact to the bottom-most WS_2 layer. The unit cell of monolayer WS_2 and 3 nm of Al_2O_3 is repeated three times to form the superlattice (Figure 1A). All three WS_2 layers are connected to the same voltage. In this case, the layers will not have the same number of injected carriers due to screening effects. The bottom-most WS_2 layer will have the largest charge injection since it lays at the interface with the gate oxide while the screening of the upper layers will depend on the Debye length of the medium. However, the Debye length of WS_2 and ALD-grown Al_2O_3 are on the scale of a few nanometers[40] and tens of nanometers,[41] respectively, so the screening effect will not be significant enough to prevent charge injection in the upper WS_2 layers. Although the same carrier density could be applied with a lower voltage by alternating the voltage applied to each WS_2 layer (i.e., the top- and bottom-most layers have a voltage applied to them while the middle layer is grounded), there were too many pinholes to apply a sizable voltage across the Al_2O_3 insulators. To overcome this challenge, the underlying SiO_2 is used as the gate oxide. The superlattice has been shown to maintain the direct band-gap nature of the constitute monolayers,[30] and an $N = 3$ structure is chosen to enhance the light-matter coupling while maintaining a large degree of tunability by modulating a single monolayer (see Figure S3).

Electro-optical properties of WS_2

The gate-tunable, complex refractive index of monolayer WS_2 on an SiO_2 (93 nm)/p^{++}-Si substrate is measured using spectroscopic

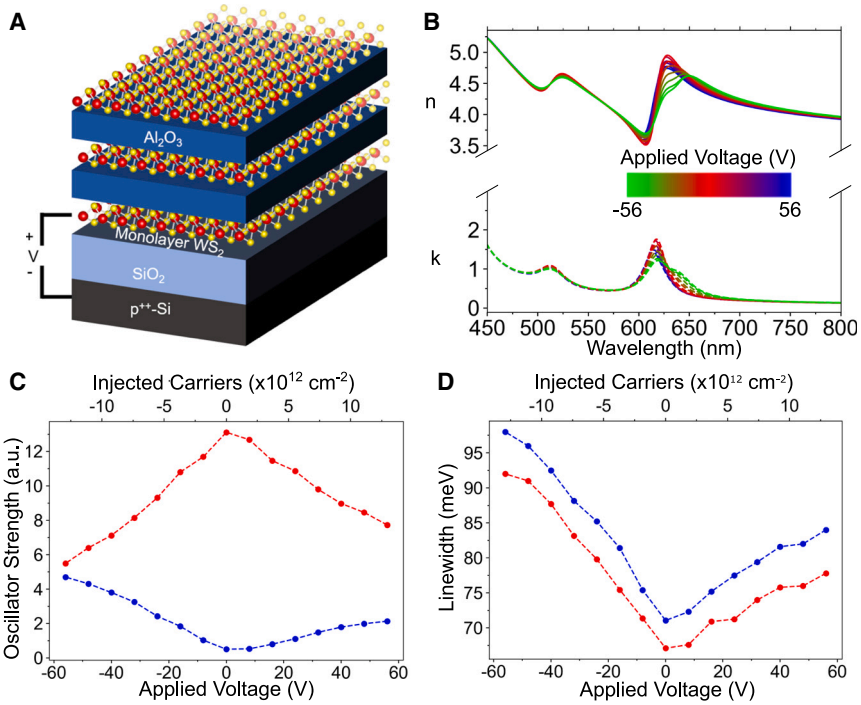

Figure 1. Gate-tunable optical properties of monolayer WS_2

(A) Schematic of the phase-tuning superlattice showing its repeated geometry and electrical contact to the WS_2 layers.

(B) The real (solid lines) and imaginary (dashed) parts of the gate-dependent refractive index measured using spectroscopic ellipsometry and voltages ranging from −56 to 56 V (8-V steps).

(C and D) The extracted gate-dependent (C) oscillator strength and (D) linewidth of the exciton and trion are from the Lorentz model. The injected carrier concentration (N_{inj}) is calculated using a parallel plate capacitor model, $N_{inj} = \frac{\varepsilon_{SiO2}\varepsilon_0 V}{et_{SiO2}}$ where t_{SiO2} is the SiO_2 thickness (93 nm), ε_{SiO2} is the permittivity of SiO_2 (3.9), e is the elementary charge, and ε_0 is the vacuum permittivity. The schematic in (A) was prepared using the VESTA software.[64]

ellipsometry to accurately model the optical properties of the sample (see section "experimental procedures" and supplemental information). The ellipsometry data are fitted to a multi-Lorentz oscillator model to extract the complex refractive index (Figure 1B). The calculated values match well with the experimental data (Figure S4). Additionally, the tunability of the monolayer is confirmed using gate-dependent photoluminescence (PL) (Figure S5). The optical properties of WS_2 are modulated by injecting charge with an applied voltage to the metal-oxide-semiconductor capacitor (MOSCap) geometry. The voltage is applied to the WS_2 layer while the p^{++}-Si substrate is grounded so a positive (or negative) applied voltage injects holes (or electrons) into the WS_2. The injected free charge modulates the screening of the electron-hole coulomb interaction of the excitons that dominate the optical properties of WS_2. The increased screening decreases the oscillator strength and increases the damping of the exciton states (Figure 1C and 1D). However, the free carriers can also bind to the neutral excitons to form charged triplet states (i.e., trions), which are seen as a new resonance that is slightly red-shifted from the exciton. The charge of the injected carriers determines the charge of trions. Interestingly, the majority of the oscillator strength lost by the exciton is gained by the trion, consistent with previous studies.[14,15,21] The trion peak is only observed when electrons are injected (V < 0 V) because the trion red-shifts away from the exciton peak allowing it to be partially resolved, but not fully resolved. However, when holes are injected, the trion blue-shifts toward the exciton, preventing its direct observation.[13,15,21]

The injected carrier concentration (N) was calculated using a parallel plate capacitor model ($N_{inj} = \frac{\varepsilon_{SiO2}\varepsilon_0 V}{et_{SiO2}}$ where t_{SiO2} is the SiO_2 thickness [93 nm], ε_{SiO2} is the permittivity of SiO_2 [3.9], e is the elementary charge, and ε_0 is the vacuum permittivity). Note that the injected carrier concentration differs from the free-carrier concentration since WS_2 is n-type under ambient conditions. The zero point for the free-carrier concentration occurs between 0 and 8 V as seen by the relatively weak modulation of the oscillator strength in this range. Additionally, the B exciton, which is the second fundamental resonance of WS_2 that results from the spin-orbit splitting of the valence and conduction bands at the K/K′ points,[42] at 510 nm shows weaker tunability than the main exciton and trion. The lower tunability is because the majority of the injected carriers occupy the lower level in the spin-orbit splitting, which partake in the main excitonic transition (A exciton) instead of the B exciton transition. Therefore, this resonance is sub-optimal for electro-optical applications.

Modulation of exciton-polaritons

When an exciton strongly couples to a cavity mode by energy being exchanged between the two states more rapidly than it is dissipated to the environment, the two states hybridize to form exciton-polaritons. Exciton-polaritons by nature confine light to a small volume due to their cavity origins and have a large degree of tunability due to their excitonic origins. This simple two-mode system is modeled using the Jaynes-Cummings model.[43] However, when a third mode is present, such as trions in our case, a three-coupled oscillator model is required where the cavity mode couples to both the exciton and trion (see supplemental information).[44]

The strength of the light-matter interactions is captured by the coupling parameter (g), and it depends on the oscillator strength (f) of the matter resonances, the number of excitonic states (N), and the mode volume (V_m) of the bare cavity $\left(g \propto \sqrt{\frac{Nf}{V_m}}\right)$.[45,46]

A single monolayer of WS_2 typically produces excitonic coupling parameters (g_x) in the range of approximately 10–30 meV depending on the cavity mode at room temperature.[47–49] However, using the transfer matrix method (see section "experimental procedures") to simulate the dispersion of our system, our system hosts an exciton coupling parameter of g_x = 78 meV and a

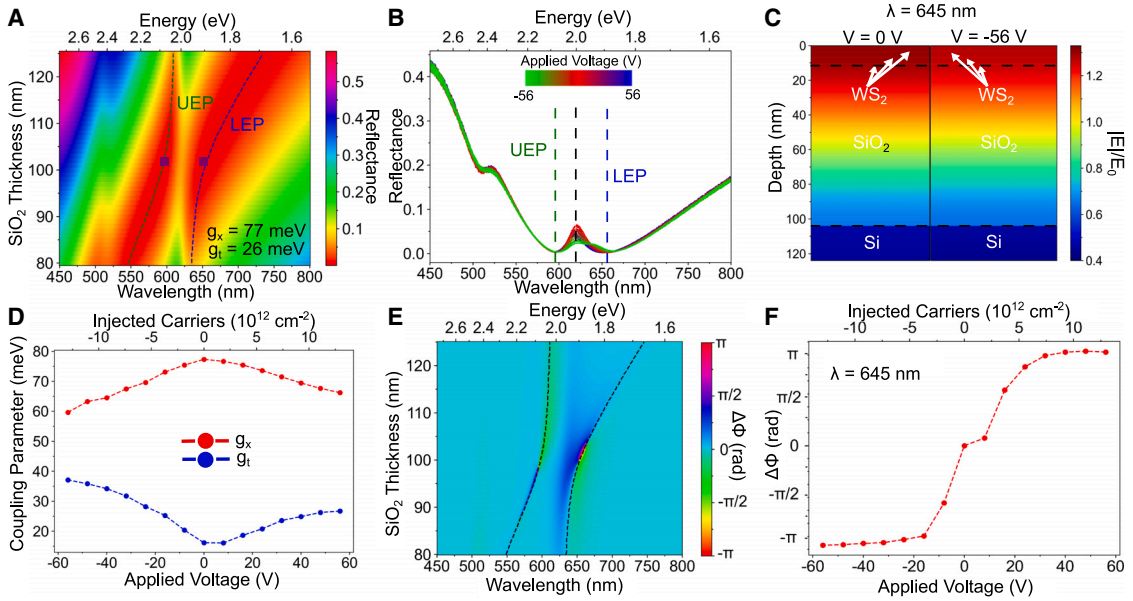

Figure 2. Simulated modulation of exciton-polaritons

(A) The simulated dispersion of TE polarized light without an applied voltage. The dispersion shows the anti-crossing behavior that is the defining featuring of excitons and cavity modes hybridizing into polaritons. The experimentally measured upper exciton-polariton (UEP) and lower exciton-polariton (LEP) wavelength of our superlattice is overlaid (purple boxes), and they agree well with theory. The UEP and LEP branches are fitted to a three-coupled-oscillator model to calculate the exciton (g_x) and trion (g_t) coupling parameters.

(B) The gate-dependent reflectance for TE polarized light at an angle of 55° with the exciton (X), UEP, and LEP labeled for the V = 0 V case.

(C) The normalized electric field profile at the operation wavelength (λ = 645 nm) for gate voltages of 0 V (left) and −56 V (right) showing the field enhancement within the WS_2 layers.

(D) The gate-dependent coupling parameters show the same trend as the oscillator strengths since $g \propto \sqrt{\frac{Nf}{V_m}}$.

(E) The modulated phase dispersion is found to closely follow the UEP and LEP demonstrating that the phase modulation is driven by the presence of the polaritons.

(F) The gate-dependent phase modulation at a single wavelength (λ = 645 nm). The phase is modulated by 2.07π radians over the range of −56– to 56 V, showing that the superlattice can fully control the phase of reflected light.

trion coupling parameter of g_t = 16 meV without an applied voltage and a 55° AOI for TE polarized light (Figure 2A). The transfer matrix method (TMM) is found to agree with the experimental superlattice demonstrating its accuracy, and the reflectance is shown to be gate tunable (Figure 2B). The large coupling parameters for monolayer WS_2 are the result of two effects. First, *N* is proportional to the number of WS_2 monolayers so the stacking process increases the coupling parameter by a factor of $\sqrt{3}$. However, this enhancement is not strong enough for exciton-polaritons to appear at normal incidence in our system. The second enhancement is that, at non-normal incidences, the interfaces become more reflective. This results in light being more efficiently trapped in the superlattice, which decreases the mode volume of the bare cavity (see Figure S6). The decreased mode volume enables the coupling parameter to be further increased to 96 meV at an incident angle of 80°, but this comes at the expense of tunability (see Figure S7). The electric field is found to be enhanced within the WS_2 layers at the operation wavelength without an applied voltage, and the electric field confinement decreases when electrons are injected (Figure 2C).

Additionally, we confirmed that all three WS_2 layers are coupled to the cavity mode by simulating a significant increase in the Poynting vector magnitude within these layers (Figure S8). The injection of charge is found to alter the dispersion of the system by both modulating the coupling parameter, through the modulation of the oscillator strengths, and by modulating the trion energy. The excitonic coupling parameter is found to decrease by 23% and g_t increases by 129% by injecting 1.3×10^{13} electrons/cm^2 in the WS_2 (Figure 2D). The reduction is large enough that the system is no longer in the strong light-matter coupling regime as evident by the lack of an exciton transparency when a voltage of −56 V is applied. Therefore, by injecting charge, the system goes from a hybridized state with exciton-polaritons to an unhybridized one with a pure exciton and pure cavity mode. Although a three-coupled oscillator should produce three polariton modes, only two polariton peaks are observed because the trion and exciton peaks are not fully resolved from one another. This results in two of the polariton modes being convoluted into one.[50]

Since exciton-polaritons are the byproduct of strong light-matter interactions, they are excellent at confining light. Therefore, the phase of reflected light is heavily influenced by the presence of exciton-polaritons. Because of this, modulating exciton-polaritons is a highly efficient method for modulating phase. This is seen in the simulated phase modulation as its dispersion is found to follow the dispersion of the unbiased superlattice (Figure 2E). Therefore, exciton-polaritons can modulate the phase of reflected light as shown in the gate-dependent phase modulation at

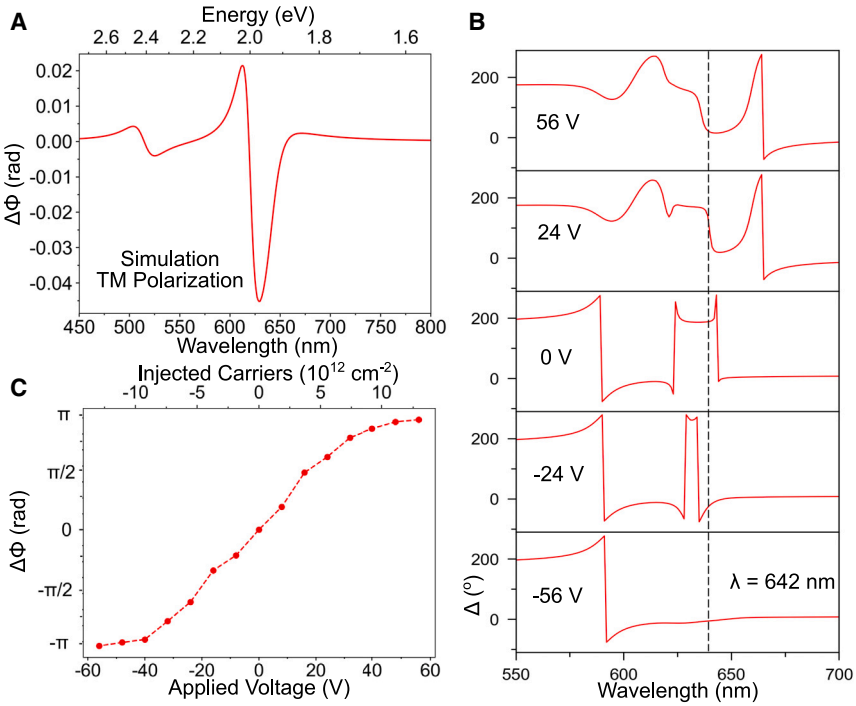

Figure 3. Experimental phase modulation

(A) The simulated phase modulation for TM polarized light in our superlattice. Since exciton-polaritons are not excited for TM polarized light, the modulation is purely excitonic, and it is limited since light is not highly confined in the superlattice by a cavity mode.

(B) The experimentally measured Δ ($\Delta = \phi_{TM} - \phi_{TE}$ where ϕ_{TM} [ϕ_{TE}] is the phase of TM [TE] reflected light) using a spectroscopic ellipsometer with an AOI of 55°. Δ is defined over the range of −100° to 260° by convention. The operation wavelength is marked by the vertical dashed line. Therefore, the sharp decreases are the result of the cyclic nature of phase.

(C) The gate-dependent phase modulation for TE polarized light at λ = 642 nm showing full 2π modulation.

λ = 645 nm where > 2π phase modulation is predicted (Figure 2F). When electrons are injected into the WS_2, the exciton oscillator strength drops, and the system goes from the hosting hybridized polaritons to weakly coupled excitons, trions, and a cavity mode. In this case, the polariton state no longer occurs below the optical band gap of WS_2, although there is still absorption due to the finite linewidth of the unperturbed modes, and the reflected light accumulates less phase. When holes are injected into the WS_2, the oscillator strength decreases, but not to the degree to enter the weak-coupling regime, causing the polariton to blue-shift. In this case, more phase is accumulated at wavelengths slightly below the unbiased polariton wavelength. This is why the wavelength with >2π is 645 nm compared to the unbiased polariton wavelength (655 nm).

Measurement of phase modulation

An $N = 3$ superlattice is fabricated to validate the predictions of our simulations (see section "experimental procedures"). We confirmed that the WS_2 maintained their high-quality monolayer properties upon stacking using Raman[51] and gate-dependent PL spectroscopy, and we confirmed the presence of exciton-polaritons using angle-dependent reflectance spectroscopy (see Figure S9).

Typical phase-modulation measurements use a Mach-Zehnder geometry to measure phase modulation in one arm relative to another unmodulated one. However, we leverage the fact that polaritons only form under TE polarized light for our chosen SiO_2 thickness. Although our superlattice does support TM mode, as predicted by theory,[23] it requires a thicker SiO_2 layer to couple to the exciton (see Figure S10). Therefore, the phase of TM light should be insensitive to gate voltage. This is validated by simulations that show that the phase modulation of TM light is 0.02 radians at λ = 642 nm over the voltage range studied here (Figure 3A).

We treated the phase of TM light as constant analogous to the reference arm of a Mach-Zehnder interferometer. The spectroscopic ellipsometer measures the phase difference between TE (ϕ_{TE}) and TM (ϕ_{TM}) light ($\Delta = \phi_{TM} - \phi_{TE}$) enabling the measurement of phase modulation of TE light (Figure 3B). Note that Δ is defined on the range of −100° to 260° by convention so the sharp decreases in Figure 3B are due to the cyclic nature of phase as opposed to a physical phenomenon. When the system is in the strong-coupling region ($V > -32$ V), the lower exciton-polariton (LEP) is present below the band gap of WS_2. This is seen as Δ highly dispersive below the exciton wavelength for all voltages except $V = -56$ V. However, at $V = -56$ V, there is no sub-gap resonance present, and, as a result, Δ is relatively flat in this range. In this case, the closest resonance is the trion, and it will dominate the optical characteristics of the superlattice. Since the trion consists purely of matter, less phase will be accumulated by incident light. As the voltage increases at λ = 642 nm, the cavity mode blue-shifts to the operating wavelength due to the weakened total oscillator strength of the exciton-trion states, and Δ decreases because of an increase in ϕ_{TE} ($\Delta = \phi_{TM} - \phi_{TE}$). This effect is strong enough for 364° phase modulation to occur at 642 nm (Figure 2C). This full 2π phase modulation requires a larger voltage than predicted by theory (Figure 2D), but this is attributed to the deposition of Al_2O_3 on top of the monolayer reducing the unbiased exciton binding energy.[12,15] Therefore, the tunability of the monolayer is reduced by the presence of the Al_2O_3. Additionally, the required charge injection and electric field strength are comparable to other phase modulators.[22,52] The use of exciton-polaritons also shows a 10× increase in phase modulation using less than one-fourth of the injected carriers of a purely excitonic WS_2 system.[21] This shows that polaritons can be leveraged to greatly enhance the efficiency of electro-optical devices.

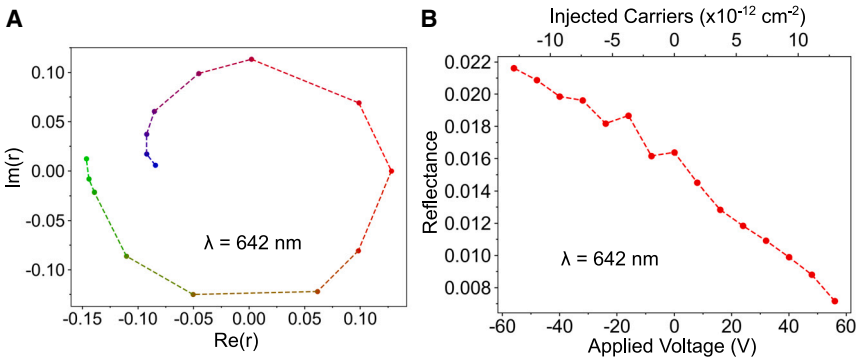

Figure 4. Loss in the superlattice phase modulator

(A) Gate-dependent reflectance spectra with an AOI of 55° for TE polarized light. The spectra were measured using both J.A. Woolam M-2000 and W-Vase ellipsometers (see section "experimental procedures"). The exciton (X), LEP, and UEP wavelengths when V = 0 V are shown.

(B) The reflection coefficient phasor (r) and (c) gate-dependent reflectance at λ = 642 nm showing the performance of the superlattice at its operating wavelength. The amplitude of the reflection coefficient phasor is measured by taken the square root of the reflectance, and its phase is measured using the gate-dependent Δ values (the phase at V = 0 V is set to 0). The gate-dependent reflectance shows that the superlattice has significant loss (17.8 dB), and the loss decreases (increases) as electrons (holes) are injected into the system.

In addition to maximum phase modulation, the loss of the system is a key metric for characterizing an electro-optical phase modulator. The gate-dependent reflectance shows the modulation of the spectra, and the largest tunability is seen at the lower polariton wavelength (Figure 2B). The reflectance spectra show two polariton modes and a reflectance minimum (absorptance maximum) at the exciton wavelength, experimentally confirming the presence of exciton-polaritons. The lower polariton also shows more tunability than the upper polariton and the B exciton (510 nm). This explains why it is the only resonance where we observe full 2π modulation. The reflection coefficient phasor is calculated using the reflectance and Δ measurements (Figure 4B). Along with the gate-dependent reflectance at the operating wavelength (Figure 4C), the reflectance is found to vary by 0.008. The reflectance is relatively constant for negative voltages since the decreasing oscillator strength and red-shifting trion energy counteract one another. However, the reflectance drops significantly for positive voltages as the polariton blue-shifts toward the operation wavelength and increases the absorptance of the system. The average loss is found to be 17.8 dB. The overall performance is quantified using the well-accepted figure of merit (FoM) of phase modulation per dB loss. This yields an FoM of 0.36 rad/dB, which is comparable to other free-space phase modulators.

Table 1 compares the performance of our superlattice with other free-space phase modulators in the visible and near infrared (λ < 1,000 nm). The FoM is found to vary from approximately 0.035 to 0.87 rad/dB for these modulators, with the exception of liquid-crystal-based modulators, and our system is near the middle with an FoM of 0.36 rad/dB. Only three of the modulators are capable of generating >π phase modulation, and both of these systems rely on bulky (several micrometers thick for the liquid crystals and millimeter thick for the perovskite) media.[19,53,54] These modulators use slow modulation methods such as thermo-optical effects that require the thermal energy to be dissipated before the next bit of information can be communicated[53,55] or the physical rotation of the molecules in liquid crystals.[19] These relatively slow speeds are adequate for human-interaction applications like displays, but they severely limit the data-transfer rate of VLC systems and the scanning speed of LiDAR. Additionally, the physical rotation of molecules leads to shorter service lifetimes of the device. Although both of these systems are excellent phase modulators, the use of subwavelength active media promises to decrease the switching energy, increase the switching speed, and allow for the integration of phase modulators into ultra-compact devices. Subwavelength phase modulators have also shown excellent performance using non-electrostatic tuning mechanisms. However, they have produced FoMs < 0.3.[56,57] However, these systems are still 100s of nanometers thick, and they do not fully unlock the advantages of the atomic limit.

At the atomic limit, phase modulators have consisted of either graphene coupled to a plasmonic metasurface[58] or planar TMDCs.[17,21] All of these phase modulators rely on a single resonance so they are limited to <π phase modulation. Graphene has been excellent for electro-optics at telecommunications wavelengths since it has a highly tunable refractive index. However, the reliance on free-carrier effects is less effective at shorter wavelengths since the Drude model depends less on the free-carrier concentration at higher energies.[59] This is why an injected carrier concentration 7.94×10^{13} cm^{-2} is needed to produce 5π/9 radians of phase modulation at λ = 760 nm while only 2.3×10^{12} cm^{-2} is needed to produce a comparable change at λ = 8.5 μm. As for TMDC-based modulators, $MoSe_2$ has been shown to modulate phase by 0.14π.[17] However, this was done at T = 4 K, which is undesirable for many electro-optical applications, and the performance rapidly decreased as temperature increased. Recent simulations have also shown that a similar $MoSe_2$/hBN superlattice structure to ours can produce 2π phase modulation per $MoSe_2$/hBN unit cell at 4 K and normal incidence.[60] An FoM of 51°°/dB was achieved in a purely excitonic system of WS_2 on an Al_2O_3/Al substrate, which outperforms our phase modulator by a factor of 2. However, this system used higher-quality, exfoliated monolayers and an ion gel to inject >5 times the number of free carriers. Therefore, a direct comparison between the two modulators to observe the performance enhancement using exciton-polaritons over bare excitons is unreasonable. Further, ion gels rely on physical movement of massive ions for gating (doping) and hence cannot respond to high frequencies of operation.[61,62] To properly compare the two system, we have re-optimized the WS_2 on Al_2O_3/Al phase modulator using our gate-tunable refractive index of WS_2 (supplemental information, Figure S11). We find that the excitonic system gives a phase modulation of 0.028π

Table 1. Comparison of phase modulators in the visible and near infrared (<1,000 nm)

System	Tuning mechanism	Operation wavelength (nm)	Injected carriers (x10^{12} cm^{-2})	Patterned?	Max phase modulation (rad)	Loss (dB)	FoM (rad/dB)
Graphene and Au metasurface[58]	electrostatic (free carriers)	760	79.4	yes	0.56π	4.19	0.42
$Al_{0.9}Ga_{0.1}As$/GaAs MQW on a DBR[56]	quantum-confined stark effect	917	–	yes	≈0.04π	9.51	≈0.13
Liquid crystals between dielectric mirrors[19]	liquid crystal rotation	532	–	no	3π	0.34	27.7
Liquid crystals coupled to a TiO_2 metasurface[54]	liquid crystal rotation	532	–	no	≈7π/4	4	≈1.37
$LiNbO_3$ metasurface (simulated)[57]	Pockels effect (free carriers)	667	–	yes	0.84π	7.7	0.34
Perovskite ($MAPBCl_3$)[53]	thermo-optic	650	–	no	≈π	≈10[a]	≈0.31
hBN-encapsulated $MoSe_2$ on graphene/SiO_2/Si at T = 4 K[17]	electrostatic (exciton)	754	9	no	0.14π	12.1	0.036
WS_2 on Al_2O_3/Al[21]	ion gel (exciton)	605	71	no	π/5	0.7	0.9
Our work	electrostatic (exciton-polariton)	642	13	no	2.02π	17.8	0.36

Comparison of the tuning mechanism, operation wavelength, injected carriers, patterning, phase modulation, and loss of several systems in literature and our work. All of the results are experimental unless otherwise indicated. MQW, multi-quantum-well; DBR, distributed Bragg reflector.
[a]Loss is simulated using the reported refractive index.

and an FoM of 0.012 rad/dB. Therefore, the use of exciton-polaritons increased the phase modulation by a factor of 71 and the FoM by a factor of 10 compared to bare excitons when normalized for WS_2 quality and carrier injection.

Phase-modulating metasurface

To demonstrate the superlattice's potential use in applications, its performance as a phase modulator in a 1D grating geometry is simulated using COMSOL Multiphysics. The 1D grating shown in Figure 5A uses the same voltage scheme as the unpatterned superlattice where each WS_2 layer has the same voltage applied to it while the Ag substrate is grounded. The Si substrate is replaced by Ag and the SiO_2 thickness is changed to 60 nm because this geometry maximizes the coupling parameter. Without any injected carriers, the dispersion shows the characteristic anti-crossing behavior of strongly coupled exciton-polaritons and a coupling parameter of 32 meV. The coupling parameter is less than the unpatterned case because we have removed some excitonic material through the patterning process, and the electric field is only contained within the center of the grating (Figure S12). However, the coupling parameter is still large enough for strongly coupled exciton-polaritons to form because the linewidth of the cavity mode is smaller than in the unpatterned case.

The presence of strongly coupled exciton-polaritons is further confirmed by the exciton transparency seen with a space of 214 nm between the gratings (Figure S13). When charge is injected into the WS_2 layers, the anti-crossing behavior disappears, and the system enters the weak-coupling regime (Figure 5C). This confirms that the system can act as a modulator. The phase dispersion is also found to follow the exciton-polariton resonance (Figure 5D). The optimal space between gratings is 226 nm for phase modulation, and the maximum phase modulation occurs near the LEP wavelength (Figure 5E). The maximum phase modulation is found to be 1.3π rad, which is less than the unpatterned case, but it can be further improved by injecting more carriers (Figure 5F). Additionally, this spatial phase modulation is large enough for LiDAR applications. The average reflectance at the optimal wavelength is 0.021, which is a 16.7-dB loss (supplemental information, Figure S14). Therefore, the FoM of the 1D grating is 0.24 rad/dB, which is still comparable to the phase modulators in Table 1.

DISCUSSION

We have demonstrated that exciton-polaritons in a WS_2 superlattice enable >360° phase modulation by electrostatic doping. The enhanced light-matter interactions of the superlattice compared to a single monolayer creates exciton-polaritons with a coupling parameter of 78 meV without the need of a top reflective layer or nanopatterning. The injection of charge into one of the monolayers in the superlattice modulates the exciton-polaritons by decreasing the exciton's oscillator strength and increasing its linewidth while also converting the system to a weakly coupled exciton-trion-polaritons. The exciton and trion coupling parameters are found to change by −23% and +129%, respectively. This process results in full 2π phase modulation of light, which is verified experimentally using spectroscopic ellipsometry.

Although the system still suffers from loss, its FoM is comparable to similar phase modulators. Additionally, when normalizing for crystal quality and carrier injection, we find that the use of exciton-polaritons increase the phase modulation by a factor of 71 and the FoM by a factor of 10 over a similar bare-exciton-based phase

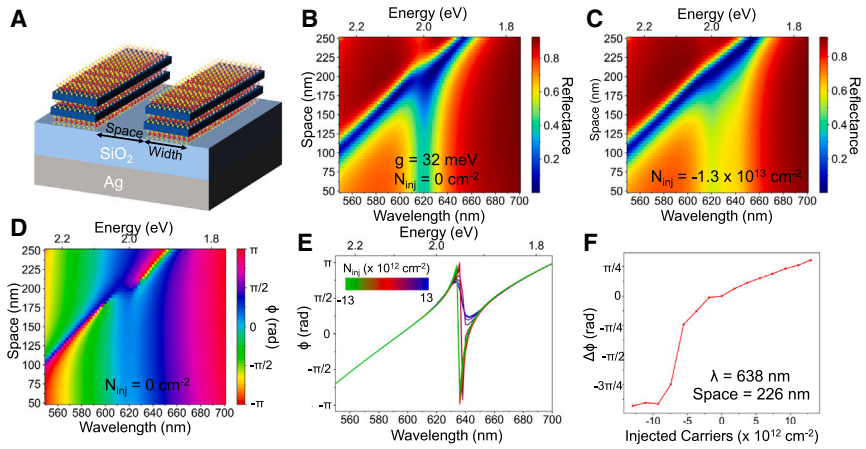

Figure 5. Simulated performance of a 1D grating

(A) Proposed design of a 1D grating phase modulator consisting of a nanopatterned, $N = 3$ superlattice on top of SiO_2 (60 nm)/Ag. The width of the gratings (set at 305 nm for all simulations) and space between them are labeled. The simulated space-dependent dispersion of the system for injected carrier concentrations of (B) 0 and (C) -1.3×10^{13} cm^{-2} showing strong (weak) coupling when no (-1.3×10^{12} cm^{-2}) carriers are injected.

(D) The phase of reflected light is found to follow the same dispersion as the exciton-polaritons in the reflectance spectra.

(E and F) (E) The phase of reflected light using the optimize space between gratings of 226 nm, and (F) the voltage-dependent phase modulation at the optimal wavelength (638 nm) and space between gratings.

modulator. This demonstrates that future phase modulators using WS_2 should focus on coupling excitons to a cavity mode in order to improve performance. Specifically, the engineering of metasurfaces using the WS_2/Al_2O_3 superlattice can reduce the loss of the phase modulator while also providing the spatial patterning that is required for LiDAR and VLCs. In this vein, we simulated a simple grated metasurface. Simulations showed that our superlattice acts as a phase modulator with an FoM of 0.24 rad/dB when it is patterned into a 1D grating for application in a LiDAR system. This work serves as a demonstration that exciton-polaritons in a WS_2 superlattice can control the properties of light in the ultrathin regime.

EXPERIMENTAL PROCEDURES

Fabrication process

The growth of monolayer WS_2 on 2″-diameter c-plane sapphire was carried out in a MOCVD system equipped with a cold-wall horizontal reactor with an inductively heated graphite susceptor with gas-foil wafer rotation (https://doi.org/10.60551/znh3-mj13). Tungsten hexacarbonyl ($W(CO)_6$) was used as the metal precursor, while hydrogen sulfide (H_2S) was the chalcogen source with H_2 as the carrier gas. The $W(CO)_6$ powder was maintained at 25°C and 400 Torr in a stainless-steel bubbler. C-plane sapphire (2″ diameter) with a nominal ±0.2° miscut toward the M-axis was used for the growths. The synthesis of WS_2 monolayer is based on a multi-step process, consisting of nucleation, ripening, and lateral growth steps, which was described previously.[37,38] In general, the WS_2 was nucleated for 30 s at 850°C, then ripened for 20 min at 850°C and 10 min at 1,000°C, and then grown for 20 min at 1,000°C, which gives rise to a coalesced monolayer across the entire 2″ wafer. During the lateral growth, the tungsten flow rate was set as 5.7×10^{-4} standard cubic centimeter per minute (sccm) and the chalcogen flow rate was set as 400 sccm, while the reactor pressure was kept at 50 Torr. After growth, the substrate was cooled in H_2S to 300°C to inhibit the decomposition of the deposited WS_2 films. Using this condition, the growth of a fully coalesced monolayer WS_2 was achieved across the 2″-sapphire substrate. The sample's detailed growth recipe and all characterization data are available at https://doi.org/10.26207/qgf7-9409.

After growth, the 2″ wafers are cleaved into 1 × 1-cm squares for the transfer process. Poly(methyl methacrylate) (PMMA) 950k A4 is spin coated on top of the samples at 2,500 rpm for 45 s, and the sample is allowed to air dry. Next, the overhanging PMMA is cleared from the edges using a razor blade, and the sample is submerged in 85°C de-ionized (DI) water until bubbles form (20–60 min). The sample is then placed on top of a 3 M solution of KOH at 85°C until the film starts to delaminate from the sapphire substrate. The sample is then manually dipped with a 45° inclination into the solution to separate the film and the substrate. The floating, PMMA-supported WS_2 monolayer is then scooped up by a glass slide and transferred to float on DI water for cleaning. The film is allowed to float for 10 min before it is transferred to a fresh DI water container. This step is repeated once more to ensure that the sample is adequately cleaned. The film is then scooped onto its desired substrate and allowed to air dry. Next, the sample is placed on a hot plate at 70°C to better adhere the film to the new substrate. The sample is then submerged in acetone on a hot plate set to 45°C to remove the PMMA. The wet-transfer processes is then completed, and the Al_2O_3 layer is deposited using a Cambridge NanotechS200 ALD system at 150°C. The electrical contacts (10 nm of Ti followed by 40 nm of Au) are deposited using an E-beam evaporator (Lesker PVD75 E-beam Evaporator).

Simulations

Simulations for the unpatterned geometry were performed using a Python script that runs a TMM simulation.[63] The refractive index of each layer was measured using ellipsometry as well as the thicknesses of the SiO_2, Al_2O_3, and WS_2 layers. The 1D grating was modeled using COMSOL Multiphysics to perform finite-difference frequency-domain (FDFD) simulations.

Spectroscopic ellipsometry

The gate-dependent refractive index and phase modulation were measured using a J.A. Woolam M-2000 ellipsometer with a focusing lens to produce a spot size ~100 μm. The results were fitted to a multi-Lorentz oscillator model (see supplemental information for details on the fitting process). As the M-2000 cannot produce normalized reflectance curves, a J.A. Woolam W-VASE ellipsometer was used to measure the angled reflectance without an applied voltage, and this spectrum was used to normalize the gate-dependent reflectance spectra of the M-2000.

RESOURCE AVAILABILITY

Lead contact

Further information and requests for resources should be directed to and will be fulfilled by the lead contact, Deep Jariwala (dmj@seas.upenn.edu).

Materials availability

This study did not generate new materials.

Data and code availability

The data presented in this paper are available from the corresponding author upon reasonable request.

ACKNOWLEDGMENTS

D.J. and J.L. acknowledge primary support for this work from the Asian Office of Aerospace Research and Development (AOARD) of the Air Force Office of

Scientific Research (AFOSR) from grant no. FA2386-21-1-4063 and the Office of Naval Research Metamaterials Program (N00014-23-1-203). D.J. also acknowledges partial support from partial support from Northrop Grumman. The authors would like to thank Zahra Fakhraai for her support with the ellipsometer. The MOCVD WS_2 monolayer samples were grown in the 2D Crystal Consortium Materials Innovation Platform (2DCC-MIP) facility at Penn State, which is supported by the National Science Foundation under NSF cooperative agreement NSF DMR-2039351. C.Y.C. acknowledges support from the NSF Graduate Research Fellowship Program (NSF GRFP, DGE-1845298). Y.-J.L. acknowledges financial support from the National Science and Technology Council of Taiwan (grant no. NSTC-110-2124-M-001-008-MY3).

AUTHOR CONTRIBUTIONS

D.J. conceived the idea. J.L. performed spectroscopic ellipsometry with the help of C.Y.C. J.L. and P.K. assembled the superlattices. C.C., N.T., S.K., and J.R. provided the MOCVD-grown WS_2 monolayers. J.L. performed the simulations and data analysis and wrote the paper. T.-Y.P. and Y.-J.L. provided theoretical support.

DECLARATION OF INTERESTS

The authors declare no competing interests.

SUPPLEMENTAL INFORMATION

Supplemental information can be found online at https://doi.org/10.1016/j.device.2024.100639.

Received: July 9, 2024
Revised: July 11, 2024
Accepted: November 13, 2024
Published: December 13, 2024

REFERENCES

1. Yu, N., and Capasso, F. (2014). Flat optics with designer metasurfaces. Nat. Mater. *13*, 139–150. https://doi.org/10.1038/nmat3839.
2. Lynch, J., Guarneri, L., Jariwala, D., and Van De Groep, J. (2022). Exciton resonances for atomically-Thin optics. J. Appl. Phys. *132*, 91102. https://doi.org/10.1063/5.0101317/2837295.
3. Li, M., Hail, C.U., Biswas, S., and Atwater, H.A. (2023). Excitonic Beam Steering in an Active van der Waals Metasurface. Nano Lett. *23*, 2771–2777. https://doi.org/10.1021/ACS.NANOLETT.3C00032.
4. van de Groep, J., Song, J.H., Celano, U., Li, Q., Kik, P.G., and Brongersma, M.L. (2020). Exciton resonance tuning of an atomically thin lens. Nat. Photonics *14*, 426–430. https://doi.org/10.1038/s41566-020-0624-y.
5. Sun, Z., Martinez, A., and Wang, F. (2016). Optical modulators with 2D layered materials. Nat. Photonics *10*, 227–238. https://doi.org/10.1038/nphoton.2016.15.
6. Li, B., Zu, S., Zhou, J., Jiang, Q., Du, B., Shan, H., Luo, Y., Liu, Z., Zhu, X., and Fang, Z. (2017). Single-Nanoparticle Plasmonic Electro-optic Modulator Based on MoS_2 Monolayers. ACS Nano *11*, 9720–9727. https://doi.org/10.1021/ACSNANO.7B05479.
7. Matheus, L.E.M., Vieira, A.B., Vieira, L.F.M., Vieira, M.A.M., and Gnawali, O. (2019). Visible Light Communication: Concepts, Applications and Challenges. IEEE Commun. Surv. Tutorials *21*, 3204–3237. https://doi.org/10.1109/COMST.2019.2913348.
8. Wang, Z., Yuan, G., Yang, M., Chai, J., Steve Wu, Q.Y., Wang, T., Sebek, M., Wang, D., Wang, L., Wang, S., et al. (2020). Exciton-enabled meta-optics in two-dimensional transition metal dichalcogenides. Nano Lett. *20*, 7964–7972. https://doi.org/10.1021/ACS.NANOLETT.0C02712.
9. Splendiani, A., Sun, L., Zhang, Y., Li, T., Kim, J., Chim, C.Y., Galli, G., and Wang, F. (2010). Emerging photoluminescence in monolayer MoS2. Nano Lett. *10*, 1271–1275. https://doi.org/10.1021/NL903868W.
10. Hsu, C., Frisenda, R., Schmidt, R., Arora, A., de Vasconcellos, S.M., Bratschitsch, R., van der Zant, H.S.J., Castellanos-Gomez, A., Hsu, C., Frisenda, R., et al. (2019). Thickness-Dependent Refractive Index of 1L, 2L, and 3L MoS_2, $MoSe_2$, WS_2, and WSe_2. Adv. Opt. Mater. *7*, 1900239. https://doi.org/10.1002/ADOM.201900239.
11. Chaves, A., Azadani, J.G., Alsalman, H., da Costa, D.R., Frisenda, R., Chaves, A.J., Song, S.H., Kim, Y.D., He, D., Zhou, J., et al. (2020). Bandgap engineering of two-dimensional semiconductor materials. npj 2D Mater. Appl. *4*, 29. https://doi.org/10.1038/s41699-020-00162-4.
12. Chernikov, A., Berkelbach, T.C., Hill, H.M., Rigosi, A., Li, Y., Aslan, O.B., Reichman, D.R., Hybertsen, M.S., and Heinz, T.F. (2014). Exciton binding energy and nonhydrogenic Rydberg series in monolayer WS2. Phys. Rev. Lett. *113*, 076802. https://doi.org/10.1103/PHYSREVLETT.113.076802.
13. Chernikov, A., Van Der Zande, A.M., Hill, H.M., Rigosi, A.F., Velauthapillai, A., Hone, J., and Heinz, T.F. (2015). Electrical Tuning of Exciton Binding Energies in Monolayer WS_2. Phys. Rev. Lett. *115*, 126802. https://doi.org/10.1103/PHYSREVLETT.115.126802.
14. Mak, K.F., He, K., Lee, C., Lee, G.H., Hone, J., Heinz, T.F., and Shan, J. (2012). Tightly bound trions in monolayer MoS2. Nat. Mater. *12*, 207–211. https://doi.org/10.1038/nmat3505.
15. Yu, Y., Yu, Y., Huang, L., Peng, H., Xiong, L., and Cao, L. (2017). Giant Gating Tunability of Optical Refractive Index in Transition Metal Dichalcogenide Monolayers. Nano Lett. *17*, 3613–3618. https://doi.org/10.1021/ACS.NANOLETT.7B00768.
16. Kravets, V.G., Wu, F., Auton, G.H., Yu, T., Imaizumi, S., and Grigorenko, A.N. (2019). Measurements of electrically tunable refractive index of MoS2 monolayer and its usage in optical modulators. npj 2D Mater. Appl. *3*, 36. https://doi.org/10.1038/s41699-019-0119-1.
17. Li, M., Biswas, S., Hail, C.U., and Atwater, H.A. (2021). Refractive Index Modulation in Monolayer Molybdenum Diselenide. Nano Lett. *21*, 7602–7608. https://doi.org/10.1021/ACS.NANOLETT.1C02199.
18. Cutolo, A., Iodice, M., Spirito, P., and Zeni, L. (1997). Silicon electro-optic modulator based on a three terminal device integrated in a low-loss single-mode SOI waveguide. J. Lightwave Technol. *15*, 505–518. https://doi.org/10.1109/50.557567.
19. Igasaki, Y., Li, F., Yoshida, N., Toyoda, H., Inoue, T., Mukohzaka, N., Kobayashi, Y., and Hara, T. (1999). High efficiency electrically-addressable phase-only spatial light modulator. Opt. Rev. *6*, 339–344. https://doi.org/10.1007/S10043-999-0339-2.
20. Wang, S.Y., and Lin, S.H. (1988). High Speed III-V Electrooptic Waveguide Modulators at lambda = 1.3 μm. J. Lightwave Technol. *6*, 758–771. https://doi.org/10.1109/50.4064.
21. Wang, Z., Sebek, M., Liang, X., Elbanna, A., Nemati, A., Zhang, N., Goh, C.H.K., Jiang, M., Pan, J., Shen, Z., et al. (2023). Greatly Enhanced Resonant Exciton-Trion Conversion in Electrically Modulated Atomically Thin WS_2 at Room Temperature. Adv. Mater. *35*, 2302248. https://doi.org/10.1002/ADMA.202302248.
22. Kim, J.Y., Park, J., Holdman, G.R., Heiden, J.T., Kim, S., Brar, V.W., and Jang, M.S. (2022). Full 2π tunable phase modulation using avoided crossing of resonances. Nat. Commun. *13*, 2103. https://doi.org/10.1038/s41467-022-29721-7.
23. Dufferwiel, S., Schwarz, S., Withers, F., Trichet, A.A.P., Li, F., Sich, M., Del Pozo-Zamudio, O., Clark, C., Nalitov, A., Solnyshkov, D.D., et al. (2015). Exciton–polaritons in van der Waals heterostructures embedded in tunable microcavities. Nat. Commun. *6*, 8579. https://doi.org/10.1038/ncomms9579.
24. Ogawa, K., Katsuyama, T., and Kawata, M. (1992). Electric field dependence of the propagation of quantum-well exciton polaritons in a waveguide structure. Phys. Rev. B *46*, 13289–13292. https://doi.org/10.1103/PhysRevB.46.13289.
25. Katsuyama, T., and Ogawa, K. (1994). Excitonic polaritons in quantum-confined systems and applications to optoelectronic devices. J. Appl. Phys. *75*, 7607–7625. https://doi.org/10.1063/1.356592.

26. Cuadra, J., Baranov, D.G., Wersäll, M., Verre, R., Antosiewicz, T.J., and Shegai, T. (2018). Observation of Tunable Charged Exciton Polaritons in Hybrid Monolayer WS_2-Plasmonic Nanoantenna System. Nano Lett. *18*, 1777–1785. https://doi.org/10.1021/ACS.NANOLETT.7B04965.

27. Dibos, A.M., Zhou, Y., Jauregui, L.A., Scuri, G., Wild, D.S., High, A.A., Taniguchi, T., Watanabe, K., Lukin, M.D., Kim, P., and Park, H. (2019). Electrically Tunable Exciton-Plasmon Coupling in a WSe_2 Monolayer Embedded in a Plasmonic Crystal Cavity. Nano Lett. *19*, 3543–3547. https://doi.org/10.1021/ACS.NANOLETT.9B00484.

28. Lee, B., Liu, W., Naylor, C.H., Park, J., Malek, S.C., Berger, J.S., Johnson, A.T.C., and Agarwal, R. (2017). Electrical Tuning of Exciton-Plasmon Polariton Coupling in Monolayer MoS_2 Integrated with Plasmonic Nanoantenna Lattice. Nano Lett. *17*, 4541–4547. https://doi.org/10.1021/ACS.NANOLETT.7B02245.

29. Park, S., Mutz, N., Schultz, T., Blumstengel, S., Han, A., Aljarb, A., Li, L.J., List-Kratochvil, E.J.W., Amsalem, P., and Koch, N. (2018). Direct determination of monolayer MoS_2 and WSe_2 exciton binding energies on insulating and metallic substrates. 2D Mater. *5*, 025003. https://doi.org/10.1088/2053-1583/AAA4CA.

30. Kumar, P., Lynch, J., Song, B., Ling, H., Barrera, F., Kisslinger, K., Zhang, H., Anantharaman, S.B., Digani, J., Zhu, H., et al. (2021). Light–matter coupling in large-area van der Waals superlattices. Nat. Nanotechnol. *17*, 182–189. https://doi.org/10.1038/s41565-021-01023-x.

31. Elrafei, S.A., Heijnen, L.M., Godiksen, R.H., and Curto, A.G. (2024). Monolayer Semiconductor Superlattices with High Optical Absorption. ACS Photonics *11*, 2587–2594. https://doi.org/10.1021/ACSPHOTONICS.4C00277.

32. Zhao, J., Fieramosca, A., Dini, K., Bao, R., Du, W., Su, R., Luo, Y., Zhao, W., Sanvitto, D., Liew, T.C.H., and Xiong, Q. (2023). Exciton polariton interactions in Van der Waals superlattices at room temperature. Nat. Commun. *14*, 1512. https://doi.org/10.1038/s41467-023-36912-3.

33. Lin, D., Lynch, J., Wang, S., Hu, Z., Rai, R.K., Zhang, H., Chen, C., Kumari, S., Stach, E., Davydov, A.V., et al. (2024). Broadband Light Harvesting from Scalable Two-Dimensional Semiconductor Heterostructures. Preprint at arXiv. https://doi.org/10.48550/arXiv.2407.05170.

34. Xu, W., Kozawa, D., Zhou, Y., Wang, Y., Sheng, Y., Jiang, T., Strano, M.S., Warner, J.H., Xu, W., Zhou, Y., et al. (2020). Controlling Photoluminescence Enhancement and Energy Transfer in WS_2:hBN:WS_2 Vertical Stacks by Precise Interlayer Distances. Small *16*, 1905985. https://doi.org/10.1002/SMLL.201905985.

35. Liu, Y., Hu, X., Wang, T., and Liu, D. (2019). Reduced Binding Energy and Layer-Dependent Exciton Dynamics in Monolayer and Multilayer WS2. ACS Nano *13*, 14416–14425. https://doi.org/10.1021/ACSNANO.9B08004.

36. Zhu, B., Chen, X., and Cui, X. (2015). Exciton Binding Energy of Monolayer WS_2. Sci. Rep. *5*, 1–5. https://doi.org/10.1038/srep09218.

37. Sebastian, A., Pendurthi, R., Choudhury, T.H., Redwing, J.M., and Das, S. (2021). Benchmarking monolayer MoS2 and WS2 field-effect transistors. Nat. Commun. *12*, 693. https://doi.org/10.1038/s41467-020-20732-w.

38. Chubarov, M., Choudhury, T.H., Hickey, D.R., Bachu, S., Zhang, T., Sebastian, A., Bansal, A., Zhu, H., Trainor, N., Das, S., et al. (2021). Wafer-Scale Epitaxial Growth of Unidirectional WS_2Monolayers on Sapphire. ACS Nano *15*, 2532–2541. https://doi.org/10.1021/ACSNANO.0C06750.

39. Kim, K.H., Oh, S., Fiagbenu, M.M.A., Zheng, J., Musavigharavi, P., Kumar, P., Trainor, N., Aljarb, A., Wan, Y., Kim, H.M., et al. (2023). Scalable CMOS back-end-of-line-compatible AlScN/two-dimensional channel ferroelectric field-effect transistors. Nat. Nanotechnol. *18*, 1044–1050. https://doi.org/10.1038/s41565-023-01399-y.

40. Wei, X., Liu, C., Qin, H., Ye, Z., Liu, X., Zong, B., Li, Z., and Mao, S. (2023). Fast, specific, and ultrasensitive antibiotic residue detection by monolayer WS_2-based field-effect transistor sensor. J. Hazard Mater. *443*, 130299. https://doi.org/10.1016/J.JHAZMAT.2022.130299.

41. Yan, D., Lu, H., Chen, D., Zhang, R., Zheng, Y., Qian, X., and Li, A. (2012). Distribution of deep-level traps at atomic-layer-deposited Al2O3/n-GaN interface. Solid State Electron. *72*, 56–59. https://doi.org/10.1016/J.SSE.2012.02.012.

42. Kozawa, D., Kumar, R., Carvalho, A., Kumar Amara, K., Zhao, W., Wang, S., Toh, M., Ribeiro, R.M., Castro Neto, A.H., Matsuda, K., and Eda, G. (2014). Photocarrier relaxation pathway in two-dimensional semiconducting transition metal dichalcogenides. Nat. Commun. *5*, 4543–4547. https://doi.org/10.1038/ncomms5543.

43. Shore, B.W., and Knight, P.L. (1993). The Jaynes-Cummings Model. J. Mod. Opt. *40*, 1195–1238. https://doi.org/10.1080/09500349314551321.

44. Lindmark, E.K., Nelson, T.R., Jr., Khitrova, G., Gibbs, H.M., Kavokin, A.V., and Kaliteevski, M.A. (1996). Three coupled oscillators: normal mode coupling in a microcavity with two different quantum wells. Opt. Lett. *21*, 994–996. https://doi.org/10.1364/OL.21.000994.

45. Andreani, L.C., Panzarini, G., and Gérard, J.-M. (1999). Strong-coupling regime for quantum boxes in pillar microcavities: Theory. Phys. Rev. B *60*, 13276–13279. https://doi.org/10.1103/PhysRevB.60.13276.

46. Larson, J., and Mavrogordatos, T. (2021). The Jaynes–Cummings Model and Its Descendants. Preprint at arxiv. https://doi.org/10.1088/978-0-7503-3447-1.

47. Lackner, L., Dusel, M., Egorov, O.A., Han, B., Knopf, H., Eilenberger, F., Schröder, S., Watanabe, K., Taniguchi, T., Tongay, S., et al. (2021). Tunable exciton-polaritons emerging from WS2 monolayer excitons in a photonic lattice at room temperature. Nat. Commun. *12*, 4933. https://doi.org/10.1038/s41467-021-24925-9.

48. Fernandez, H.A., Withers, F., Russo, S., and Barnes, W.L. (2019). Electrically Tuneable Exciton-Polaritons through Free Electron Doping in Monolayer WS_2 Microcavities. Adv. Opt. Mater. *7*. https://doi.org/10.1002/ADOM.201900484.

49. Gu, J., Chakraborty, B., Khatoniar, M., and Menon, V.M. (2019). A room-temperature polariton light-emitting diode based on monolayer WS_2. Nat. Nanotechnol. *14*, 1024–1028. https://doi.org/10.1038/s41565-019-0543-6.

50. Rana, F., Koksal, O., Jung, M., Shvets, G., Vamivakas, A.N., and Manolatou, C. (2021). Exciton-Trion Polaritons in Doped Two-Dimensional Semiconductors. Phys. Rev. Lett. *126*, 127402. https://doi.org/10.1103/PHYSREVLETT.126.127402.

51. Zeng, H., Liu, G.B., Dai, J., Yan, Y., Zhu, B., He, R., Xie, L., Xu, S., Chen, X., Yao, W., and Cui, X. (2013). Optical signature of symmetry variations and spin-valley coupling in atomically thin tungsten dichalcogenides. Sci. Rep. *3*, 1608. https://doi.org/10.1038/srep01608.

52. Biswas, S., Grajower, M.Y., Watanabe, K., Taniguchi, T., and Atwater, H.A. (2021). Broadband electro-optic polarization conversion with atomically thin black phosphorus. Science *374*, 448–453. https://doi.org/10.1126/SCIENCE.ABJ7053.

53. Handa, T., Tahara, H., Aharen, T., and Kanemitsu, Y. (2019). Large negative thermo-optic coefficients of a lead halide perovskite. Sci. Adv. *5*, eaax0786. https://doi.org/10.1126/SCIADV.AAX0786.

54. Hu, Y., Ou, X., Zeng, T., Lai, J., Zhang, J., Li, X., Luo, X., Li, L., Fan, F., and Duan, H. (2021). Electrically Tunable Multifunctional Polarization-Dependent Metasurfaces Integrated with Liquid Crystals in the Visible Region. Nano Lett. *21*, 4554–4562. https://doi.org/10.1021/ACS.NANOLETT.1C00104.

55. Liu, S., Feng, J., Tian, Y., Zhao, H., Jin, L., Ouyang, B., Zhu, J., and Guo, J. (2022). Thermo-optic phase shifters based on silicon-on-insulator platform: state-of-the-art and a review. Front. Optoelectron. *15*, 9. https://doi.org/10.1007/S12200-022-00012-9.

56. Wu, P.C., Pala, R.A., Kafaie Shirmanesh, G., Cheng, W.H., Sokhoyan, R., Grajower, M., Alam, M.Z., Lee, D., and Atwater, H.A. (2019). Dynamic beam steering with all-dielectric electro-optic III–V multiple-quantum-well metasurfaces. Nat. Commun. *10*, 3654. https://doi.org/10.1038/s41467-019-11598-8.

57. Gao, B., Ren, M., Wu, W., Cai, W., and Xu, J. (2021). Electro-optic lithium niobate metasurfaces. Sci. China Phys. Mech. Astron. *64*, 240362. https://doi.org/10.1007/S11433-021-1668-Y.

58. Wan, Y., An, Y., Tao, Z., and Deng, L. (2018). Manipulation of surface plasmon resonance of a graphene-based Au aperture antenna in visible and near-infrared regions. Opt Commun. *410*, 733–739. https://doi.org/10.1016/J.OPTCOM.2017.11.042.

59. Feigenbaum, E., Diest, K., and Atwater, H.A. (2010). Unity-order index change in transparent conducting oxides at visible frequencies. Nano Lett. *10*, 2111–2116. https://doi.org/10.1021/NL1006307.

60. Li, M., Michaeli, L., and Atwater, H.A. (2024). Electrically Tunable Topological Singularities in Excitonic Two-Dimensional Heterostructures for Wavefront Manipulation. ACS Photonics *11*, 3554–3562. https://doi.org/10.1021/ACSPHOTONICS.4C00397.

61. Lee, J., Kaake, L.G., Cho, J.H., Zhu, X.Y., Lodge, T.P., and Frisbie, C.D. (2009). Ion gel-gated polymer thin-film transistors: Operating mechanism and characterization of gate dielectric capacitance, switching speed, and stability. J. Phys. Chem. C *113*, 8972–8981. https://doi.org/10.1021/JP901426E.

62. Wang, D., Zhao, S., Yin, R., Li, L., Lou, Z., and Shen, G. (2021). Recent advanced applications of ion-gel in ionic-gated transistor. npj Flex. Electron. *5*, 13. https://doi.org/10.1038/s41528-021-00110-2.

63. Pettersson, L.A.A., Roman, L.S., Inganäs, O., and Inganä, O. (1999). Modeling photocurrent action spectra of photovoltaic devices based on organic thin films. J. Appl. Phys. *86*, 487–496. https://doi.org/10.1063/1.370757.

64. Momma, K., and Izumi, F. (2011). *VESTA 3* for three-dimensional visualization of crystal, volumetric and morphology data. 0021-8898 *44*, 1272–1276. https://doi.org/10.1107/S0021889811038970.